Small Structures

small structures

www.small-structures.com

RESEARCH ARTICLE OPEN ACCESS

Charged Microdroplets Enable Surfactant-Free Janus Nanoparticles from Homogeneous Precursors

Saloni Gupta[1] | Radhika Bharathi Sankar[1] | Anirban Som[1] | Keerthana Unni[1] | Sujan Manna[1] | Prakrati Patidar[1] | Depanjan Sarkar[1,2] | Pradeep Thalappil[1,2,3]

[1]DST Unit of Nanoscience (DST UNS) & Thematic Unit of Excellence (TUE), Department of Chemistry, Indian Institute of Technology Madras (IITM), Chennai, India | [2]Centre of Excellence on Molecular Materials and Functions, Department of Chemistry, Indian Institute of Technology Madras (IITM), Chennai, India | [3]International Centre for Clean Water, IIT Madras Research Park, Chennai, India

Correspondence: Depanjan Sarkar (depanjansarkar@gmail.com) | Pradeep Thalappil (pradeep@iitm.ac.in)

Received: 5 February 2026 | **Revised:** 5 February 2026 | **Accepted:** 24 March 2026

Keywords: ambient synthesis | composition-control | Janus nanoparticles | microdroplets | size control

ABSTRACT

Precise size control of nanoparticle size and uniformity has remained an unmet challenge in microdroplet-based synthesis, despite recent progress in this area. Here, we demonstrate that electric field–mediated reaction confinement and evaporation dynamics provide a robust handle for size and morphology focusing of nanoparticles in electrosprayed microdroplets. By exploiting this coupling between droplet lifetime, internal electric field gradients, and solute redistribution, we obtained highly monodisperse nanoparticles (8–30 nm) under ambient conditions. Under specific reaction conditions, we observed the formation of fused biphasic (groundnut-shaped) morphologies via electric field-driven phase segregation during rapid solvent evaporation in the microdroplets. Building on this mechanistic insight, we extended the strategy to bimetallic systems and, for the first time, achieved direct, surfactant-free synthesis of Janus Ag–Au nanoparticles from homogeneous precursors, without postsynthetic modification. This work establishes a generalizable principle of tunability based on controlled droplet electrodynamics, enabling both precise size focusing and compositional anisotropy. Such control over nanoparticle architecture opens new directions for scalable design of dual-site catalysts and multifunctional sensors, demonstrated here in the form of surface-enhanced Raman spectroscopy.

1 | Introduction

Janus nanoparticles, asymmetrically structured nanomaterials with distinct surface properties on opposing faces or domains, have emerged as a powerful platform for advanced applications in catalysis, sensing, and drug delivery [1–5]. Unlike homogeneous nanoparticles or alloys, Janus structures enable synergistic functionality through spatially segregated domains, yet their synthesis typically requires complex emulsion templates, surfactants, or multistep seed-mediated growth. Developing direct routes from simple homogeneous precursors remains a major challenge. Beyond composition, precise size control over nanoparticles (NPs) remains equally critical, as it governs catalytic activity, plasmonic response, and biocompatibility [6, 7]. For NPs containing 300–400 atoms or more, traditional bulk-phase synthesis methods, despite decades of refinement, struggle to achieve monodispersity due to uncontrolled nucleation, growth, and aggregation dynamics [6]. Even with surfactants or capping agents, bulk methods often yield polydisperse distributions. Factors such as simultaneous nucleation and growth, Ostwald ripening, and heterogeneous reaction environments contribute to significant size variation. Although strategies such as surfactant modulation, precursor dosing, or pH and reductant adjustment can partially narrow size distributions, achieving true monodispersity in bulk systems remains a challenge [8]. This persistent limitation not only complicates fundamental studies but also restricts the utility of NPs in applications that demand uniformity, such as plasmonic sensors with narrow resonance bands or catalysts with site-specific activity. To address these, new

synthetic methodologies with improved precision must be developed.

Ambient-charged microdroplets offer a unique solution to both challenges. Recent advances in chemical and materials research using ambient-charged microdroplets have opened unique opportunities to overcome the limitations of traditional bulk synthesis [9]. In recent years, ambient charged microdroplets have emerged as a powerful platform for organic and nanomaterial synthesis, offering unprecedented control over reaction environments [10–14]. The ambient nature of this method allows for easy customization of synthetic parameters (e.g., droplet size, charge density, flow rate, and solvent composition) to achieve desired outcomes. Our research group, a pioneer in synthesizing nanomaterials using charged microdroplets, has demonstrated that even slight adjustments to the deposition environment, such as introducing a conducting mesh or an air-water interface, can dramatically alter the morphology of synthesized materials [15, 16]. Our group has demonstrated that charged microdroplets enable facile fabrication of NPs [17], nanowires (NWs) [15, 18], nanorods (NRs) [19], and nanosheets (NSs) [20–22], bimetallic/alloy nanomaterials [15], and oxide microstructures directly from precursor salt solutions [23], without the need for surfactants, reductants, or high-temperature processing, key limitations of traditional methods. As femtoliter-scale reactors, ambient charged microdroplets undergo rapid solvent evaporation, charge redistribution, and electric field-driven dynamics during their flight [24]. These conditions accelerate reaction kinetics by orders of magnitude, enhance interfacial phenomena, and suppress uncontrolled aggregation, enabling precise control over nucleation and growth [25]. The extreme internal pressures and electric fields within charged droplets further drive spontaneous redox reactions, phase segregation, and self-assembly processes that typically require harsh reagents or templates in bulk systems. Despite these advantages, the potential of ambient-charged microdroplets to synthesize complex nanostructures, such as Janus NPs, from homogeneous precursors remains underexplored. Similarly, their ability to reconcile monodispersity with scalability, a critical gap in nanomaterials research, has yet to be fully realized.

Here, we report the first synthesis of Janus nanoparticles (Ag-Au and Au-Pd) directly from homogeneous mixed-metal salt solutions using ambient charged microdroplets, without surfactants, reductants, or templates. By tuning electrospray parameters (tip-to-substrate distance, voltage, concentration), we achieve simultaneous control over size (8–30 nm), shape (polyhedral to single-crystal), and composition. Electric-field-driven phase segregation during rapid evaporation enables unprecedented structural precision, as validated by size-dependent Surface-enhanced Raman spectroscopy (SERS) enhancement and demonstrated scalability under ambient conditions.

2 | Results and Discussion

2.1 | Size Control of Ag NPs

Figure 1A presents a schematic representation of the tip-to-substrate–dependent electrospray deposition (ESD) setup. For these experiments, a 1 mM aqueous solution of silver acetate (AgOAc) was prepared and loaded into a glass emitter with a tip diameter of 25–30 µm. The custom-made nanoelectrospray ionization (nESI) source was secured to a stable burette stand using a clamp for controlled deposition. Prior to the experiments described here, the effects of precursor concentration and spray duration were systematically optimized (details provided in a

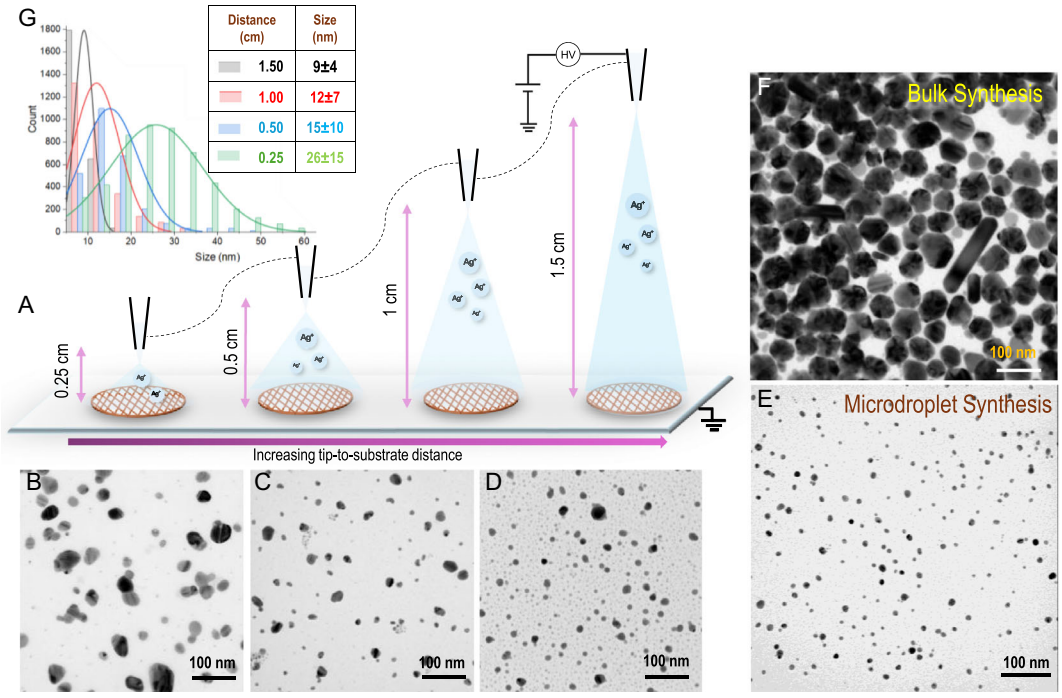

FIGURE 1 | (A) Schematic representation of the tip-to-substrate distance-dependent electrospray deposition experiment. TEM images of Ag NPs synthesized at a tip-to-substrate distance of (B) 0.25, (C) 0.5, (D) 1.0, and (E) 1.5 cm. (F) TEM image of Ag NPs synthesized using the standard bulk method. (G) Size distribution of the NPs synthesized using microdroplets under various conditions.

later section). Based on these preliminary results, all subsequent experiments were conducted using a 1 mM precursor solution and a spray duration of 30 min to ensure reproducibility and optimum deposition quality. Four clean transmission electron microscopy (TEM) grids were placed on a clean indium tin oxide (ITO) slide, which was then grounded using a crocodile clip. The ITO slide containing the TEM grids was placed on a moving stage with XYZ movement capacity. A scale was fixed beside the spray tip to measure the tip-to-substrate distance. At the beginning, the distance from the tip to the TEM grid substrate was kept at 1.5 cm, and the electrospray deposition was started by applying a high potential in the range of 2–2.5 kV. The stability of the electrospray was visually tested using a low-power laser light. The deposition was carried out for 30 min without any disruption. After 30 min, the moving stage was shifted to the next grid, and the distance from the tip to the substrate was adjusted to 1 cm, followed by deposition experiments under identical conditions. The procedure was replicated for the subsequent two sample sets while adjusting the deposition distance to 0.5 and 0.25 cm, respectively. While reducing the tip-to-substrate distance, the applied voltage was slightly adjusted to avoid any flickering of the spray or liquid jet formation due to the enhanced electric field. A voltage-dependent experiment was also performed (discussed in a later part) to confirm the effect of applied voltage on the formed particles. After completion of the experiments, TEM imaging was performed for each sample. Multiple images were captured from different areas of the grid and at different magnifications to achieve proper size distributions of the NPs. Figure 1B–E shows representative TEM images collected from the samples made at tip-to-substrate distances of 0.25, 0.5, 1.0, and 1.5 cm, respectively.

As shown in the images, particle size increases as the deposition distance decreases. This inverse relation may be due to the fact that at lower deposition distances, the droplet size was significantly larger compared to the higher distances. While droplet sizes in flight were not directly measured, the trend in NP size with tip-to-substrate distance aligns with the established electrospray principles and the literature on evaporation-driven Coulombic fission. Shorter distances preserve larger primary droplets, while longer flight paths enable successive fission into smaller daughter droplets. To demonstrate the advantage of controllability in microdroplet-based synthesis over conventional bulk synthesis, we performed a standard bulk preparation of citrate-protected Ag NPs. In this experiment, the established synthetic protocol was followed, involving a reaction at 100°C with continuous stirring for 60 min. Figure 1F presents the TEM image of the obtained Ag NPs. As is evident, despite the use of sodium citrate as a capping agent and elevated reaction temperature, the particle size distribution was nonuniform. The bulk synthesis serves as a widely used benchmark showing that even under optimized conditions for forming citrate-capped nanoparticles at elevated temperatures, the size distribution remains significantly broader than in the microdroplet-derived samples, thereby emphasizing the controllability of the microdroplet route (Figure 1E). The size distribution plot shown in Figure 1G also supports the observation from the TEM images. As evident from the size distribution plot, at a lower tip-to-substrate distance (0.25 cm), the majority of the NPs were found to be sized between 25–30 nm, in comparison to the higher distance (1.5 cm), where the particle size was within a narrow range of 8–10 nm. Hence, these results demonstrate that it is indeed possible to engineer targeted size distributions of desired NPs using ambient microdroplets. The size distribution was calculated from a set of twenty TEM images at a 100 nm scale bar (as represented in Figure 1) using the ImageJ image processing software. Tunable Ag NPs can be synthesized on a large area, as shown in a TEM image in Figure S1. This striking finding underscores the potential of the microdroplet approach and motivates further investigation into the underlying phenomenon.

2.2 | Role of Precursor Concentration

The relationship between the concentration of the precursor solution and the resultant NP size was investigated. A series of ESD experiments was conducted using increasing concentrations of aqueous AgOAc solutions (0.01, 0.1, 1, 5, and 10 mM), with all other conditions held constant (tip-to-substrate distance: 1 cm; tip size: 25 μm; deposition time: 30 min; applied potential: 2.2–2.4 kV). In each case, the formation of Ag NPs was confirmed by TEM images, as shown in Figure S2. The images clearly demonstrate that both the size and density of the NPs increase with higher AgOAc concentrations. This trend can be attributed to two main factors. First, higher salt concentrations increase the viscosity and surface tension of the solution, resulting in larger initial droplets during the electrospray process. These larger droplets contain more Ag^+ ions, which, upon solvent evaporation and nucleation, yield larger NPs due to the greater mass of material per droplet. Second, elevated precursor concentrations provide more Ag^+ ions in each droplet, promoting rapid nucleation followed by growth as excess ions aggregate around nuclei before solvent evaporation is complete. Although concentration-dependent size control of the NPs is possible, this approach has a limitation: at lower concentrations, the particle density is very low, making it difficult to fabricate surfaces with enough small NPs for any applications. Therefore, we conclude that controlling the tip-to-substrate distance provides a more effective strategy for the controlled fabrication of NPs.

2.3 | Role of Applied Potential

Applied potential is another critical parameter in ambient microdroplet-based synthesis of nanomaterials. To examine its effect on NP size, a voltage-dependent experiment was conducted using a 1 mM aqueous solution of AgOAc, electrospray deposited at a 1 cm tip-to-substrate distance for 30 min. Two different applied potentials, 2 and 3 kV, were tested. TEM images of the resulting NPs are shown in Figure S3. As expected, the NPs formed at the higher applied potential were comparatively smaller in size compared to those formed at the lower potential. This can be attributed to the increased voltage, enhancing the charge density of the solution, which promotes Coulombic fission. This process splits the droplets into smaller units, reducing the solute and solvent content per droplet and accelerating evaporation, ultimately yielding smaller NPs. However, voltage-dependent size control is not preferred in our experiments for two main reasons: at higher voltages, the nESI tip is prone to damage, resulting in unstable sprays, and experiments involving higher voltages carry increased risk factors and require greater energy consumption.

2.4 | Role of Deposition Time

Another important consideration in optimizing the method is whether the NPs coalesce on the substrate during deposition, potentially leading to the formation of larger particles. To investigate this, a time-dependent deposition study was performed using a 0.1 mM aqueous AgOAc solution. TEM images were obtained after 10 and 30 min of deposition (Figure S4A,B, respectively). The images indicate that the NP sizes are comparable in both cases, suggesting that deposition time has minimal effect on the size distribution of the particles. Hence, we conclude that distance-dependent size control is the most effective and reliable approach for engineering targeted NPs in this case.

2.5 | Distance-Dependent Size Control of Au NPs

To assess whether distance-dependent size tuning is general across noble metals, we performed analogous ESD experiments using 1 mM aqueous $Au(OAc)_3$ under identical conditions. In contrast to Ag, Au NPs exhibited a reverse trend in size with tip-to-substrate distance: smaller particles were obtained at shorter distances (0.25 cm), while larger sizes appeared at longer distances (1.5 cm) (Figure S5). This behavior is attributed to the higher reduction potential and multistep reduction pathway of Au^{3+}, which, combined with differences in surface diffusion and growth kinetics, shifts the balance between nucleation and growth compared to Ag. These results highlight that while microdroplet electrodynamics (distance, voltage, and concentration) provide a common handle for size control, the exact distance–size relationship is metal-specific and is governed by precursor redox chemistry and interfacial kinetics.

2.6 | Aspects of Droplet Physics

The initial droplet diameter for an electrospray is given by $D_0 \propto (\gamma Q^2/\varpi\sigma V^2)^{1/3,}$ where D_0 = initial droplet diameter, γ = surface tension, Q = liquid flow rate, σ = charge on droplet surface, and V = applied voltage. The charge density, assuming a uniform beam model, on the droplets can be approximated as $\rho_e \propto I/(4\pi r^2 v)$, where ρ_e = charge density, I = deposition current, r = droplet radius, v = droplet velocity, and $4\pi r^2$ = droplet surface area. Table 1 summarizes the impact of the parameters on the NPs formed.

2.7 | Electric Field-Driven Biphasic Nucleation

During HRTEM analysis of Ag NPs synthesized at a tip-to-substrate distance of 0.25 cm, an intriguing structural feature was observed. As shown in Figure 2A, the NPs exhibited irregular morphologies with varying image contrast (mainly because of their orientational variability), suggestive of complex internal structures. Closer inspection revealed multifaceted geometries with distinct lattice plane junctions (Figure 2B), indicating that crystallites of different orientations had coalesced within individual particles during the electrospray deposition process. We speculate that the extremely short deposition distance facilitated ultra-rapid nucleation of Ag^+ ions, leaving insufficient time for the growing crystals to fully reorganize into uniform lattice arrangements. Consequently, the resulting particles displayed multiple crystal facets and heterogeneous lattice alignments. Remarkably, among these structures, we frequently encountered configurations reminiscent of Janus particles. An example is presented in Figure 2C, where two distinct Ag domains are joined to form a single biphasic (groundnut-shaped) NP. When the tip-to-substrate distance was increased, the deposited NPs exhibited improved crystallinity, often forming single-crystalline structures, as exemplified in Figure 2D–F for a tip-to-substrate distance of 1.5 cm. This observation prompted us to address a new challenge, exploring compositional controllability in microdroplet-based synthesis, which is examined in the following section of this manuscript.

2.8 | Synthesis of Ag-Au Janus NPs

To investigate compositional control within microdroplet-based synthesis, we prepared a homogeneous aqueous solution containing 1 mM each of AgOAc and gold(III) acetate [$Au(OAc)_3$] and subjected it to ESD at a tip-to-substrate distance of 0.25 cm. Remarkably, this process yielded heterostructured Ag–Au Janus NPs, as evidenced by large-area TEM imaging (Figure 3A). High-resolution TEM imaging revealed a distinct lattice junction between Ag and Au, as shown in Figure 3B. High-angle annular dark-field scanning transmission electron microscopy (HAADF-STEM) analyses of both clustered (Figure 3C) and individual NPs (Figure 3D) provided clear visualization of the biphasic Janus architecture. The apparent core–shell-like features arise from the two-dimensional projection of NPs in different orientations. Furthermore, elemental mapping through energy-dispersive X-ray spectroscopy (EDS) confirmed the spatial segregation of Ag and Au domains within individual NPs. Figure 3E presents the EDS elemental maps of multiple Ag–Au Janus NPs, while Figure 3F displays the corresponding EDS spectra collected from different regions of the same particles. The spectrum from area 1 (green trace) corresponds to an Au-rich region, whereas area 2 (red trace) represents an Ag-rich region. These results clearly

TABLE 1 | Effects of single-parameter variations (others held constant) on electrospray-generated droplets and nanoparticles. ↑ = Increase in value; ↓ = Decrease in value; γ = surface tension; TOF = time-of-flight.

	Effect on the droplets			
Parameter varied	**Droplet size**	**Charge density (σ)**	**TOF**	**NP outcome**
Distance ↓	Larger ↑	Negligible effect	Shorter ↓	Larger NP ↑
Voltage ↑	Smaller ↓	Higher ↑	Shorter (Negligible)	Smaller NP ↓
Concentration ↑	Larger ↑ (Higher γ)	Negligible effect	Negligible effect	Larger NP ↑ Higher density ↑
Time of deposition ↑	Negligible effect	Negligible effect	Negligible effect	Density ↑
	*In all experiments, only one parameter was varied at a time while the others were kept constant			

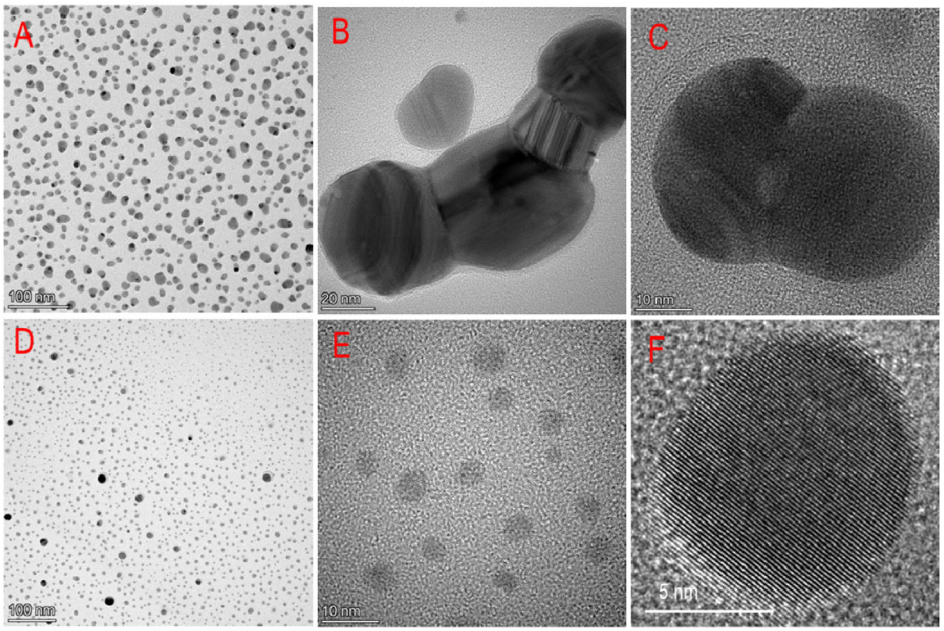

FIGURE 2 | TEM images of Ag NPs synthesized at a tip-to-substrate distance of 0.25 cm. (A) Large area image, (B) multifaceted geometries with distinct lattice plane junctions, and (C) bi-lobal (groundnut-shaped) silver NP. TEM images of Ag NPs synthesized at a tip-to-substrate distance of 1.5 cm. (D) Large area image, (E) HRTEM of the NPs, and (F) HRTEM of a single Ag NP showing Ag (111) lattice plane.

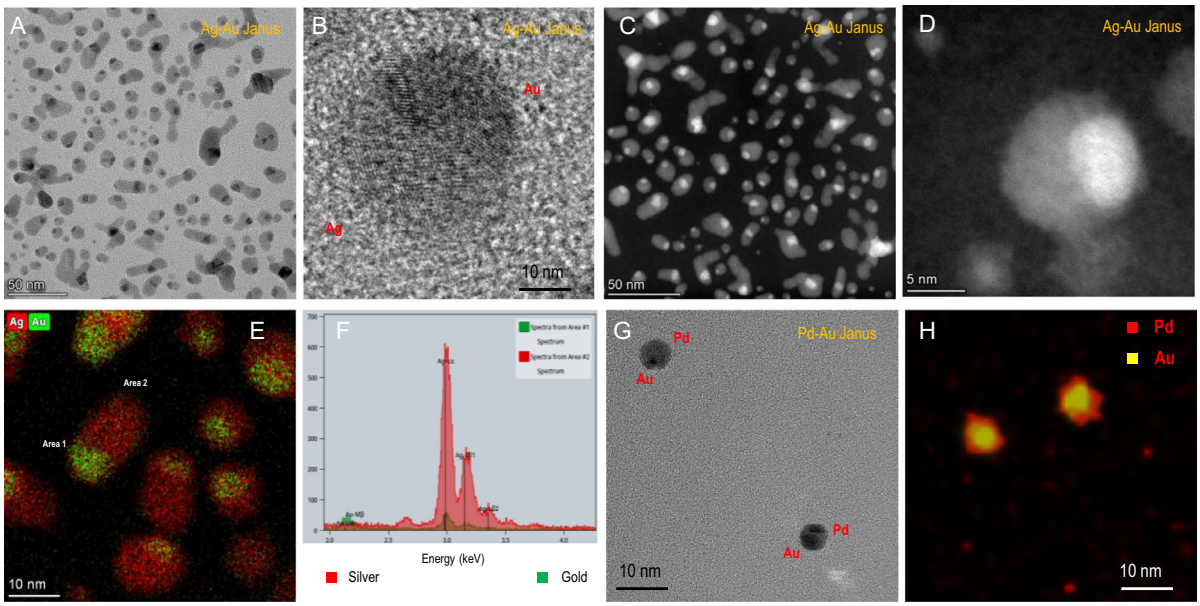

FIGURE 3 | (A) Large area TEM image of Ag-Au Janus NPs. (B) HRTEM of a single Ag-Au Janus NP demonstrating a sharp lattice boundary. (C) Large area HAADF-STEM image of Ag–Au Janus NPs showing clear phase separation, with brighter and darker regions corresponding to Au- and Ag-rich domains, respectively. (D) HAADF-STEM image of Ag–Au single Janus NP. Apparent core-shell-looking structures seen are due to the 2D projection of different orientations of the nanoparticles. (E) EDS-mapped image of Ag-Au NPs; red color represents the Ag part, and green color represents the Au part. (F) EDS spectrum collected from the different parts of a single Janus NP; area 1 (green trace) represents Au, and area 2 (red trace) represents Ag. (G) TEM image of Pd-Au Janus NPs. (H) EDS-mapped image of Pd-Au NPs; red color represents the Pd part, and yellow color represents the Au part.

demonstrate that the two metals are spatially localized, forming a well-defined Janus structure.

2.9 | Mechanistic Origin of Janus Formation

We propose that Janus Ag-Au NP formation under short tip-to-substrate distances (0.25 cm) arises from electric field-directed phase segregation during kinetic trapping in charged microdroplets. The strong electric fields ($\approx 10^8$–10^9 V/m) drive rapid, simultaneous reduction of homogeneous Ag^+/Au^{3+} precursors (no external reducing agents are used in our case), but with a distinct thermodynamics–kinetics balance: although Au^{3+} has a higher standard reduction potential ($E^0 = +1.50$ V) than Ag^+ ($E^0 = +0.80$ V), its multistep reduction ($Au^{3+} \rightarrow Au^+ \rightarrow Au^0$)

and stronger interfacial preference make its overall reduction kinetics in charged microdroplets slower and more surface–localized than the one–step $Ag^+ \rightarrow Ag^0$ process, yielding spatially distinct nuclei within the same droplet. Radial field gradients further amplify asymmetry, directing lower-charge Ag^+ toward droplet interiors and higher-charge Au^{3+} toward charged interfaces, as evidenced by biphasic Ag-only particles at identical conditions (Figure 2). Ultra-fast evaporation (<1 ms lifetime) and suppressed Ostwald ripening freeze the domains before atomic interdiffusion/alloying, as confirmed by HAADF-STEM (Figure 3C–F) and spatially resolved EDS, which show Ag-rich (78% ± 6% Ag) vs. Au-rich (65% ± 8% Au) domains with sharp lattice boundaries (Figure 3B).

2.10 | Extension to Pd-Au Janus NPs

Further to check the universality of the method demonstrated here, we tested Janus NPs for the Pd-Au system. Under identical conditions, using 1:1 mM $Pd(OAc)_2/Au(OAc)_3$ produces Pd-Au Janus NPs (Figure 3G), where Pd^{2+} ($E^0 = +0.95$ V) segregation mirrors Ag behavior, confirming that the mechanism requires only sufficient reduction potential difference ($\Delta E^0 > 0.1$ V). This surfactant-free, ambient synthesis of Janus structures from homogeneous precursors represents a generalizable electrodynamic principle for compositional anisotropy, previously unreported in microdroplet science.

2.11 | Fabrication of Target-Specific Substrate for SERS

To explore the practical applications of our size-controlled NPs, their performance as SERS substrates was evaluated. For fabricating any substrate, scalability is an important factor. UV–Vis (Figure S6) and dynamic light scattering (DLS) (Figure S7) spectra of the as-synthesized Ag NPs, obtained using the microdroplet technique, were measured to confirm scalability. The DLS data show a higher size distribution, mainly because NPs undergo agglomeration typical of uncapped noble metal particles in the solution during extended collection. These measurements were performed only to assess solution-phase scalability for substrate fabrication; primary nanoparticle size control was established from TEM analysis of the deposited substrates (Figure 1). This ambient microdroplet-based synthesis technique has offered a facile, material-efficient approach to fabricating SERS-active substrates, thereby enhancing sustainability through minimized reagent consumption. Ag NPs synthesized at varying tip-to-substrate distances were tested for their SERS activity using 10 μM methylene blue as a probe molecule. A clear trend has been observed in which substrates composed of smaller NPs, formed at longer distances (1.5 cm), have exhibited significantly enhanced Raman signal intensities compared to those synthesized at shorter distances (0.25 cm). This enhancement can be attributed to the size-dependent plasmonic properties of the NPs: as particle size has decreased, localized surface plasmon resonance has been strengthened, thereby amplifying the electromagnetic fields that drive SERS enhancement [26, 27]. Figure 4 displays the corresponding Raman spectra, confirming that microdroplet-based control of NP size has directly translated to tunable and improved SERS substrate performance. Additionally, Ag–Au Janus nanoparticles were evaluated as SERS substrates and exhibited Raman signal enhancements comparable to those of the size-optimized Ag-only substrates (Figure S8), indicating that introducing compositional anisotropy does not compromise plasmonic performance. This has demonstrated the capability of our microdroplet approach not only for precise NP synthesis but also for the sustainable fabrication of high-performance plasmonic sensing platforms.

3 | Conclusion

In conclusion, this study demonstrates a versatile and sustainable microdroplet-based electrospray deposition technique for the

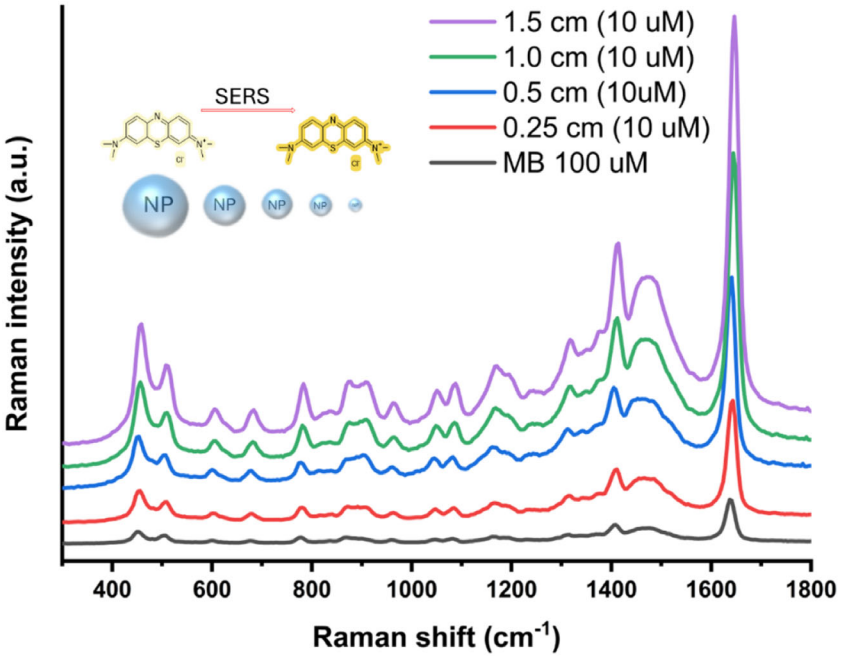

FIGURE 4 | Raman spectra of methylene blue collected on Ag NP substrates created using microdroplet-based synthesis at various tip-to-substrate distances, showing the enhancement in the Raman intensity for smaller NPs.

controlled synthesis of noble metal NPs with tunable size, shape, and composition. By precisely adjusting easily controllable experimental parameters such as tip-to-substrate distance, an ambient, surfactant-free, and reagent-efficient approach has been established, enabling the formation of uniquely structured NPs, including multifaceted Ag particles, Ag–Au, Pd-Au Janus heterostructures, and size-controlled Ag and Au NPs, where Au displays an opposite distance–size trend relative to Ag due to its distinct redox and growth kinetics. The intricate interplay among deposition conditions, droplet dynamics, nucleation kinetics, and precursor solution chemistry governing NP formation within charged microdroplets has been elucidated. Importantly, the fabrication of highly uniform and compositionally controlled NPs has been directly translated into enhanced functional performance, as exemplified by the superior SERS activity of size-optimized Ag substrates synthesized via this method. A detailed experimental and theoretical study is needed in the future to gain deeper insight into the mechanisms of Janus particle formation and the ongoing processes within these unique microdroplet environments. This work has advanced fundamental understanding of microdroplet-mediated nanomaterial synthesis and established a scalable platform for producing tailored plasmonic materials with minimized environmental impact. It is anticipated that the methodology and mechanistic insights presented here will be further explored and broadly adopted across diverse fields, including catalysis and sensing.

4 | Experimental Section

4.1 | Materials

Silver acetate (AgOAc, ≥99%) and gold(III) acetate ($[Au(OAc)_3]$, ≥99%) were purchased from Sigma Aldrich, India, and used as received without further purification. Methylene blue was also purchased from Sigma Aldrich, India, and used as received without further purification. Ultrapure water (resistivity > 18.2 MΩ·cm) was used for all aqueous solution preparations. Analytical grade sodium citrate was obtained from RANKEM for bulk-phase synthesis comparison experiments.

4.2 | Preparation of Precursor Solutions

For the synthesis of NPs using microdroplets, aqueous solutions of AgOAc (1 mM, unless specified otherwise) were freshly prepared and loaded into nESI glass electrospray emitters (tip diameter 25–30 μm). For the synthesis of Janus NPs, homogeneous solutions containing 1 mM AgOAc and 1 mM $[Au(OAc)_3]$ were prepared by sonication in water for 15 min.

4.3 | Electrospray Deposition Setup

A custom-built nanoelectrospray ionization (nESI) source was securely mounted on a burette stand. To enable precise control over deposition parameters, a home-built XYZ movable stage was used to adjust the position and height of the spray. The emitter was positioned at variable tip-to-substrate distances (0.25, 0.5, 1.0, or 1.5 cm) from the collection substrate. For all experiments, four TEM grids were placed on a clean ITO-coated glass slide, which was grounded using a crocodile clip to ensure effective charge dissipation during deposition. A scale was fixed beside the emitter to measure tip-to-substrate distances accurately. Electrospray deposition was performed under ambient laboratory conditions at room temperature. A high potential (2–2.5 kV, adjusted as necessary to prevent liquid jetting) was applied to induce electrospray from the emitter. Spray stability was monitored visually using a low-power laser pointer. The standard deposition time for each sample was 30 min, with the stage shifted sequentially to expose new grids for each distance regime.

4.4 | Synthesis Parameter Optimization

Precursor concentration studies were performed by varying AgOAc solution concentration (0.01, 0.1, 1, 5, and 10 mM) at a fixed tip-to-substrate distance (1 cm), tip diameter (25 μm), deposition time (30 min), and applied voltage (2.2–2.4 kV). Voltage-dependent experiments employed 2 and 3 kV with 1 mM AgOAc to examine effects on particle morphology and size. Deposition time optimization was conducted by comparing samples deposited for 10 and 30 min using 0.1 mM AgOAc at a 1 cm tip-to-substrate distance.

4.5 | Bulk-Phase Synthesis of Ag NPs

For control experiments, Ag NPs were synthesized in bulk using established protocols. Sodium citrate (10 mM) was added to boiling aqueous $AgNO_3$ (1 mM), and the reaction was maintained at 100°C with continuous stirring for 1 h. Resulting NPs were isolated by centrifugation, washed with ultrapure water, and analyzed using TEM.

4.6 | Characterization of the NPs

Synthesized NPs were characterized by TEM to determine size, morphology, and structural features. TEM grids were imaged at multiple locations and magnifications; particle size distributions were obtained using ImageJ software from at least twenty images per sample. High-angle annular dark-field scanning transmission electron microscopy (HAADF-STEM) and EDS were employed for elemental mapping and confirmation of Ag-Au Janus morphology. UV–visible (UV–vis) spectroscopy and DLS analysis were performed to confirm particle formation, size distributions, and material scalability. SERS measurements were performed using 10 μM methylene blue as a probe molecule to assess substrate performance.

Acknowledgments

We acknowledge the ANRF Science and Engineering Research Board (SERB), the Department of Science and Technology (DST), and the Government of India for their research funding. T.P. acknowledges the financial support of SERB SUPRA (SPR/2021/000439). We acknowledge the support of the Centre of Excellence on Molecular Materials and Functions under the institution of Eminence scheme of IIT Madras. TEM measurements were performed at the ANRF SERB National Facility for Cryo-Electron Microscopy, IIT Madras.

Funding

Department of Science and Technology, Ministry of Science and Technology, India; Science and Engineering Research Board (SPR/2021/000439).

Conflicts of Interest

The authors declare no conflicts of interest.

Data Availability Statement

Data are available from the corresponding authors upon request.

References

1. A. Walther and A. H. E. Müller, "Janus Particles: Synthesis, Self-Assembly, Physical Properties, and Applications," *Chemical Reviews* 113 (2013): 5194.

2. G. Agrawal and R. Agrawal, "Janus Nanoparticles: Recent Advances in Their Interfacial and Biomedical Applications," *ACS Applied Nano Materials* 2 (2019): 1738.

3. Y. Song and S. Chen, "Janus Nanoparticles: Preparation, Characterization, and Applications," *Chemistry – An Asian Journal* 9 (2014): 418.

4. Z. Rahiminezhad, A. M. Tamaddon, S. Borandeh, and S. S. Abolmaali, "Janus Nanoparticles: New Generation of Multifunctional Nanocarriers in Drug Delivery, Bioimaging and Theranostics," *Applied Materials Today* 18 (2020): 100513.

5. M. Lattuada and T. A. Hatton, "Synthesis, Properties and Applications of Janus Nanoparticles," *Nano Today* 6 (2011): 286.

6. N. T. K. Thanh, N. Maclean, and S. Mahiddine, "Mechanisms of Nucleation and Growth of Nanoparticles in Solution," *Chemical Reviews* 114 (2014): 7610.

7. B. Mekuye and B. Abera, "Nanomaterials: An Overview of Synthesis, Classification, Characterization, and Applications," *Nano Select* 4 (2023): 486.

8. K. K. Rudman, S. Hosseini, K. Chatterjee, B. Johnson, and S. E. Skrabalak, "Sonoelectrosynthesis of Monodisperse Metal Nanoparticles," *Nanoscale* 14 (2022): 6471.

9. J. Ghosh and R. G. Cooks, "Mass Spectrometry in Materials Synthesis," *TrAC Trends in Analytical Chemistry* 161 (2023): 117010.

10. X. Yan, "Emerging Microdroplet Chemistry for Synthesis and Analysis," *International Journal of Mass Spectrometry* 468 (2021): 116639.

11. J. K. Lee, S. Banerjee, H. G. Nam, and R. N. Zare, "Acceleration of Reaction in Charged Microdroplets," *Quarterly Reviews of Biophysics* 48 (2015): 437.

12. X. Jia, J. Wu, and F. Wang, "Water-Microdroplet-Driven Interface-Charged Chemistries," *JACS Au* 4 (2024): 4141.

13. D. Xia, H. Xie, Z. Fu, and J. Chen, "Microdroplets: An Overlooked "Engine" of Chemistry in Air," *Environmental Science & Technology* 59 (2025): 6357.

14. D. T. Holden, N. M. Morato, and R. G. Cooks, "Aqueous Microdroplets Enable Abiotic Synthesis and Chain Extension of Unique Peptide Isomers from Free Amino Acids," *PNAS* 119 (2022): e2212642119.

15. D. Sarkar, M. K. Mahitha, A. Som, et al., "Metallic Nanobrushes Made Using Ambient Droplet Sprays," *Advanced Materials* 28 (2016): 2223–2226, https://doi.org/10.1002/adma.201505127.

16. A. Li, Q. Luo, S.-J. Park, and R. G. Cooks, "Synthesis and Catalytic Reactions of Nanoparticles Formed by Electrospray Ionization of Coinage Metals," *Angewandte Chemie International Edition* 53 (2014): 3147.

17. A. Li, Z. Baird, S. Bag, et al., "Using Ambient Ion Beams to Write Nanostructured Patterns for Surface Enhanced Raman Spectroscopy," *Angewandte Chemie International Edition* 53 (2014): 12528–12531, https://doi.org/10.1002/anie.201406660.

18. D. Sarkar, A. Som, and T. Pradeep, "Catalytic Paper Spray Ionization Mass Spectrometry with Metal Nanotubes and the Detection of 2,4,6-Trinitrotoluene," *Analytical Chemistry* 89 (2017): 11378–11382, https://doi.org/10.1021/acs.analchem.7b02288.

19. K. S. Aswathi, K. Unni, S. Mukhopadhyay, et al., "Ambient Microdroplet Synthesis of Pt and Pt–Cu Nanorods from Homogeneous Solutions for Electrocatalytic Nitrate Reduction," *Nanoscale Horizons* (2026), https://doi.org/10.1039/D5NH00572H.

20. D. Sarkar, R. Singh, A. Som, et al., "Electrohydrodynamic Assembly of Ambient Ion-Derived Nanoparticles to Nanosheets at Liquid Surfaces," *Journal of Physical Chemistry C* 122 (2018): 17777–17783, https://doi.org/10.1021/acs.jpcc.8b04169.

21. D. Sarkar, B. Mondal, A. Som, et al., "Holey MoS_2 Nanosheets with Photocatalytic Metal Rich Edges by Ambient Electrospray Deposition for Solar Water Disinfection," *Global Challenges* 2 (2018): 1800052.

22. D. Sarkar, A. Som, K. Unni, S. Manna, and P. Thalappil, "Interfacial Growth of Large Area Single-Crystalline Silver Sheets Through Ambient Microdroplets," *Small* 21 no. 28 (2024): 2400159.

23. K. Unni, J. Shantha Kumar, A. Som, D. Sarkar, and T. Pradeep, "From Solution to Microstructures in Minutes: Microdroplet-Derived Stand-Alone TiO_2 Surfaces for Simultaneous Water Harvesting and Treatment," *ACS Sustainable Chemistry & Engineering* 12 (2024): 11957.

24. G. Rovelli, M. I. Jacobs, M. D. Willis, R. J. Rapf, A. M. Prophet, and K. R. Wilson, "A Critical Analysis of Electrospray Techniques for the Determination of Accelerated Rates and Mechanisms of Chemical Reactions in Droplets," *Chemical Science* 11 (2020): 13026.

25. K. R. Wilson and A. M. Prophet, "Chemical Kinetics in Microdroplets," *Annual Review of Physical Chemistry* 75 (2024): 185.

26. D. M. Solís, J. M. Taboada, F. Obelleiro, L. M. Liz-Marzán, and F. J. García de Abajo, "Optimization of Nanoparticle-Based SERS Substrates through Large-Scale Realistic Simulations," *ACS Photonics* 4 (2017): 329.

27. J. P. Camden, J. A. Dieringer, Y. Wang, et al., "Probing the Structure of Single-Molecule Surface-Enhanced Raman Scattering Hot Spots," *Journal of the American Chemical Society* 130 (2008): 12616.

Supporting Information

Additional supporting information can be found online in the Supporting Information section.